



## Sensitivity study of the SA-DDES shielding function

Downloaded from: <https://research.chalmers.se>, 2024-03-13 07:29 UTC

Citation for the original published paper (version of record):

Siggeirsson, E., Andersson, N., Wallin, F. (2018). Sensitivity study of the SA-DDES shielding function. AIAA Aerospace Sciences Meeting, 2018(210059). <http://dx.doi.org/10.2514/6.2018-1355>

N.B. When citing this work, cite the original published paper.

# Sensitivity study of the SA-DDES shielding function

Siggeirsson, Elias M. V. <sup>\*</sup> and Andersson, Niklas <sup>†</sup>  
*Chalmers University of Technology, Gothenburg, SE-41296, Sweden*

Wallin, Fredrik <sup>‡</sup>  
*GKN Aerospace Engine Systems Sweden, Trollhättan, SE-46181, Sweden*

**In this paper the performance of the Delayed Detached Eddy Simulation (DDES) turbulence model is analyzed for a nozzle blade that serves as a Pre-Swirl (PSW) in an experimental test rig. The DDES model is based on the one-equation turbulence model developed by Spalart and Allmaras. The focus is put on evaluating how well the shielding function, an essential part in the DDES model, protects the boundary layer around the PSW. This study is a part of a larger project, where future ambitions are to apply the DDES model to the whole experimental rig configuration. Preliminary simulations on the PSW showed that the shielding function did not protect the boundary layer as intended. Modification to the DDES model, proposed in the literature where a coefficient in the shielding function is altered, were therefore implemented and tested with promising results. The modification results in a better model performance for the PSW. For that reason the modified model will be considered in future simulations of the full experimental rig.**

## I. Nomenclature

*Greek/Roman*

$\tilde{\nu}$	=	Spalart-Allmaras viscosity, $m^2 s^{-1}$
$d$	=	wall distance, $m$
$f_d$	=	DDES shielding function
$\tilde{d}$	=	length scale, $m$
$C_{DES}$	=	filter width factor
$\Delta$	=	subgrid length scale, $m$
$\Delta_0$	=	focus region cell size
$y_{wall}^+$	=	wall normal coordinate at the wall
$\Delta x, \Delta y, \Delta z$	=	grid spacing, $m$

*Subscript*

$t$	=	stagnation properties
$in$	=	inlet flow property
$out$	=	outlet flow property

## II. Introduction

Over the past decades, air traffic has increased rapidly, leading to a global increase in CO<sub>2</sub> emissions along with other green-house gases. Increase in emission has been locally slowed down with newer aircraft [1], but unfortunately only temporary, as all air traffic forecasts point to a rapid growth [2, 3]. To make air traffic more sustainable over a longer period of time, continuous performance improvements are needed. One major aspect in improving the aircraft performance is to increase the aircraft engine efficiency.

---

<sup>\*</sup>PhD Student, Department of Mechanics and Maritime Sciences

<sup>†</sup>Associate Professor, Department of Mechanics and Maritime Sciences

<sup>‡</sup>R&T Program Manager, Dept 9600-TLab3

Improvement of engine efficiency has been quite successful over the past decades, specially with the increased usage of Computational Fluid Dynamics (CFD). One improvement is the development of the high bypass-ratio turbo-fan engine with large fans and high pressure-ratio engine cores, which combines the high efficiency, high sub-sonic aircraft velocities and low noise levels. Further efficiency improvements are however getting harder to achieve with current design methodologies. In the design process the engine components are usually divided into several modules, where each module is optimized separately with simplified interaction. Ghisu et al. [4] showed that optimizing modules in isolation from each other could result in a sub-optimal design. The sub-optimal design can unfortunately lead to an expensive redesign late in the design process. However, by including more components in a single design process, the risk can be lowered substantially. This integrated design process takes the advantages of lowering the need of simplified or modelled interaction between components, resulting in a more optimal solution earlier in the design process [4, 5].

One component of the engine, that has not been optimized to the same extent as surrounding components is the intermediate compressor duct (ICD), which connects the upstream low pressure (LPC) and downstream high pressure compressors (HPC). Still, there have been some successful studies where the objective was to optimize or analyse the ICD [6–10], resulting in shorter and lighter engines, with aggressive flow guidance as a result of larger radial offset and shorter axial spacing. The interactions between the duct and the surrounding modules have however not been addressed in the same way, even though it has been shown that by doing so can improve the performance substantially [4]. Gao et al. [11] studied the effect of inlet conditions on compressor duct and noted that for a specific duct design, the exit flow and total pressure recovery coefficient was negatively affected with increasing inlet velocity. Bailey et al. [12] showed that when using engine representative inlet conditions, the risk of separation in the duct is reduced due to re-energized boundary layers. This means that an analysis of an integrated design approach can give substantial information that can be vital in making the module more efficient. Britchford et al. [13, 14] analysed in detail the internal flow field of a "clean" annular S-shaped duct, using experiments and CFD. These studies were performed to understand the flow physics and behavior in more detail. In both studies, fully developed annulus duct flow was applied as an inlet boundary condition for the S-shaped duct.

Figure 1 shows an example of a turbo-fan engine, with a zoom in on the ICD. The LPC and HPC can be seen as well as the radial offset between the two, where the duct is used to guide the flow from a larger radius to smaller one. To be able to analyze the flow physics of the compressor duct in detail, an experimental rig has been built at GKN Aerospace in Trollhättan, Sweden. Fig. 2 illustrates how the test section of the experimental rig is set up. It consists of Pre-Swirlers (PSW), bleed pipe, Outlet Guide Vanes (OGV) and struts, where all but the PSW are representative of real engine components. The PSW is placed there to generate realistic inlet conditions to the ICD, which would otherwise be generated by the upstream compressor components. The OGV:s are integrated into the duct to achieve shorter length [9] and the bleed pipe is used to ensure stable operating conditions for part-speed operations by allowing for different amount of massflow through the LPC and HPC.

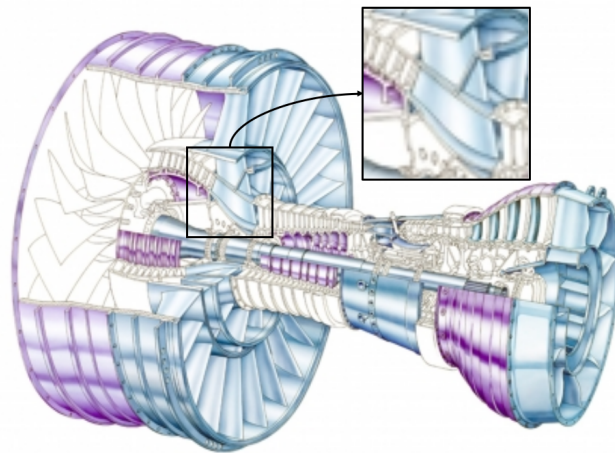


**Fig. 1 Aircraft engine.**

One constraint, in applying a more integrated duct design approach is computational power as including more components results in much higher computational demand. That demand increases even further when 3D CFD

simulations are considered. Furthermore, to be able to take full advantages of the CFD simulation and the integrated design, a step towards Large Eddy Simulation (LES) needs to be taken in order to get a better representation of flow separation and other complicated flow behaviour that is not captured by the more common Reynolds Averaged Navier-Stokes (RANS) models. In the present study, to limit the computational cost to some extent, the hybrid LES/RANS model Delayed Detached Eddy Simulation (DDES), introduced by Spalart et al. [15] is used, as it combines the abilities of the LES in resolving the transient flow features of the main flow and the RANS model in calculating the attached near wall behaviour with moderate grid density.

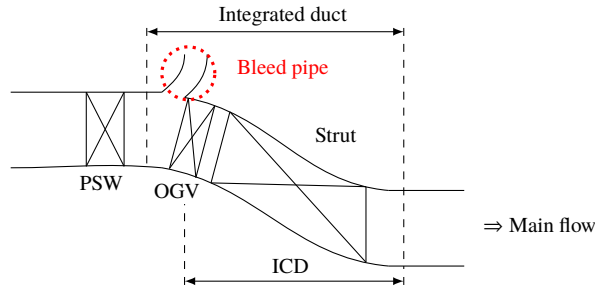


**Fig. 2 Schematic of the integrated compressor duct design.**

In the process of simulating the full ICD experimental rig, problems were encountered regarding the DDES shielding function. The shielding function was not protecting the boundary layer as it should near the blade, where the mesh had relatively fine cells in the streamwise direction. In a literature study, recent studies [16–18] were found where a similar behaviour for different kind of flows was encountered. Both Ashton et al. [17] and Probst et al. [18] suggested an alteration to the default model which will be discussed further in the coming section.

In this paper the DDES turbulence model, based on the Spalart-Allmaras (S-A) one-equation model, is used to simulate the PSW sub-module from the integrated design. This is done to analyze the default and the modified shielding function in the DDES model. The current study will serve as a vital initial step in verifying that the simulation tools are capable in performing properly before the simulations on the full integrated ICD configuration are conducted.

### III. Numerical method

#### A. Flow solver

The finite volume in-house CFD solver for compressible flow, called G3D::Flow\*, is used. It is based on a family of codes developed by Eriksson [19]. The solver is developed and maintained at the Division of fluid dynamics at Chalmers University of Technology. It uses three-stage Runge-Kutta time marching method with a third-order accurate upwind-biased scheme for all convective terms and a second-order accurate compact centered scheme for all diffusive terms. For more details on the numerical scheme, see Eriksson [19] or Andersson et al. [20].

The hybrid RANS/LES model, the DDES model, based on the S-A one-equation turbulence model is used. The main motivation for using a hybrid model is that it combines the advantages the LES capability in resolving the large scales of the transient main flow and the RANS capability in resolving the boundary layer with relatively low computational cost.

#### B. DDES

The original DES model was introduced by Spalart et al. [21] as a hybrid between LES and the one equation S-A RANS turbulence model [22]. Initially the model was only presented for a 2D application but extended to 3D by Shur et al. [23]. In that study the performance of the DES model gave a promising result which lead to a wide usage. It was however shown that for grids with stream-wise grid spacings of similar size as the boundary layer a premature switching from RANS to LES could occur. This was the motivation for the new and improved DES, called DDES [15]. In the DDES model the switching between RANS and LES is no longer governed only by the grid density but also the

\*Code home page: <https://nikander.github.io/g3dflow/>



flow itself. This has greatly improved the application of the model as less time can be spent in fulfilling the strict grid requirements of the DES model.

The improvements in the DDES model is a shielding function that protect the boundary layer from premature switching into LES. The DDES model introduces a parameter  $r_d$

$$r_d = \frac{\tilde{\nu}}{\sqrt{U_{i,j}U_{i,j}}\kappa^2 d^2} \quad (1)$$

where  $\tilde{\nu}$  is the S-A viscosity,  $U_{i,j}$  are the velocity gradients,  $\kappa$  is the von Kármán constant and  $d$  is the distance to the wall. The  $r_d$  function is equal to 1 in the logarithmic layer and falls gradually towards zero at the edge of the boundary layer. The  $r_d$  function is then used as a part of the boundary layer shielding function  $f_d$ ,

$$f_d = 1 - \tanh \left[ (C_1 r_d)^{C_2} \right]. \quad (2)$$

where  $C_1 = 8$  and  $C_2 = 3$ .

The  $f_d$  function is designed to be 0 in the RANS region but 1 in the LES region, where  $r_d \ll 1$ . The length scale, proposed by the original DES model was only based on the wall distance and the grid spacing,

$$\tilde{d}_{DES} = \min(d, C_{DES}\Delta) \quad (3)$$

but this can result in a grid induced separation. Therefore a modified length scale was introduced as

$$\tilde{d}_{DDES} = d - f_d \max(0, d - C_{DES}\Delta) \quad (4)$$

When  $f_d = 0$ , the model behaves like a RANS model, whereas  $f_d = 1$  results in the original DES model shown in Eq. (3). Shur et al. [23] compared the S-A as a Sub-Grid-Scale (SGS) model to the Smagorinsky SGS model and experimental data. There, a good agreement was achieved using the filtering factor  $C_{DES} = 0.65$  for the DDES model, simulating isotropic turbulence.

The coefficients in the  $f_d$  function, Eq. (2), were calibrated using a flat-plate boundary layer but recent studies have shown that some modifications might be needed for it to perform well for specific problems, specially geometries where strong stream wise gradients are present. Ashton [16] presented work for a three element airfoil, where a problem regarding the shielding function was encountered. The conclusion was that even though the DDES model was applied, the stream-wise and span-wise grid sizes were too fine. The fine mesh, in addition to strong pressure gradients over curved surfaces, caused the shielding function to break down and allowed for LES mode inside the boundary layer. Ashton et al. [17] made a calibration study where the sensitivity to the  $C_1$  coefficient was made for the DDES model using different computational setup. For a zero-pressure gradient flat plate case, the values  $C_1 = 10, 12, 16, 20$  were tested. Large improvements were observed for all modifications, when looking at the boundary layer viscosity. All modified versions then resulted in the same solution. For an Ahmed body, the gray-area between the two different modes causes the separation to be over predicted as  $C_1$  is increased. This is because too high viscosity damps out the fluctuations, resulting in a larger separation. Probst et al. [18] encountered a similar problem for a simple airfoil. In their opinion a coarser mesh was not an option as high resolution in the stream-wise direction was required to be able to capture the adverse pressure gradient over the wing. Instead, they suggested a slight modification to the  $f_d$  function where the value of  $C_1$  was increased from 8 to 16, shown in Eq. (5).

$$f_{d,16} = 1 - \tanh \left[ (16r_d)^3 \right] \quad (5)$$

This shows a loophole in the generality of the DDES model, which was supposed to shield the boundary layer with more ambiguity regarding finer grids. The modification of  $C_1 = 16$  will be used in the current study as it has proven to provide proper shielding for wing profiles, the gray-area problem has to be kept in mind though.

Furthermore, it has been shown that when the S-A model is used as a base model for DDES, the  $f_{i2}$  term should be excluded in the equations. The reason is that it has the tendency to cause the boundary layer to stay laminar over the geometry on finer grids [24]. In addition, the S-A model is implemented with the negative  $\tilde{\nu}$  treatment, suggested by Spalart et al. [25] and the DDES model includes the low-Reynolds number correction published by Spalart et al. [15]. In the following, the modified model will be referred to as DDES<sub>16</sub> whereas the original model will be referred to as DDES<sub>8</sub>.

### C. Computational setup

Figure 3 presents the computational domain used in this study. Since the aim is to analyze the performance of the turbulence model for the isolated PSW geometry, only a single blade passage is used. The channel is defined by the upper and lower surfaces, shroud and hub, respectively. Rotational periodicity is applied to the periodic boundaries (not shown for clarity). For post-processing, two surfaces are defined. The mid radius surface (MR) around the blade and the Front Traverse surface (FT) downstream of the blade, near the outlet of the domain, both are shown in the figure.

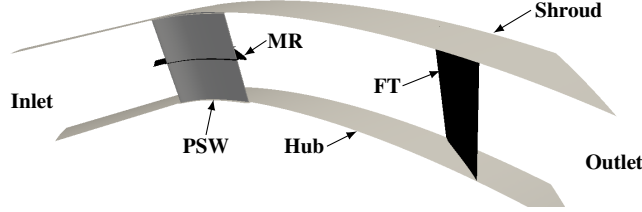


**Fig. 3 3D representation of the computational setup.**

The boundary conditions employed are presented in Table 1. The inlet is defined by the static and total pressure and the S-A turbulent viscosity. A previous simulation is conducted of a clean annular duct to obtain the inlet profiles. At the outlet, a static pressure is specified. When initializing the solver for the coarser mesh, a linear incrementation between the inlet and outlet is used for all variables. For the finer mesh, the initial condition is interpolated from the coarser, converged solution. This saves both computational resources and valuable time.

**Table 1 Boundary conditions.**

$p_{t,in}$	$p_{in}$	$\tilde{\nu}_{in}$	$p_{out}$
76650 Pa	75476 Pa	$5\nu$	75743 Pa

### D. Computational Grid

The computational grid is a structured mesh satisfying the wall normal distance of  $y^+ < 1$ . In the free-stream flow field, the cell sizes in the span-wise and stream-wise directions are a couple of orders of magnitude larger than in the wall-normal direction at the wall. The free-stream cell size is set to make sure that the grid is fine enough to be able to resolve the large scales and the transient behaviour of the main flow in LES mode. In Table 2 the total number of cells are presented for the mesh used in this study along with the wall normal and free-stream cell sizes, in the stream-wise, span-wise and tangential directions.

**Table 2 Mesh statistics.**

Mesh	Number of Cells	$y_{wall}^+$	$\Delta x^+$	$\Delta y^+$	$\Delta z^+$
PSW	2.8M	$< 1$	$(400 - 1200)y^+$	$(400 - 800)y^+$	$(400 - 800)y^+$

In Fig. 4, the mesh for the blade passage and the lower part of the blade is presented (every other grid line is shown for better visualisation). The view is from downstream of the blade, pointed towards the trailing edge. The structured O-grid topology is visible around the blade. By comparing the two, a small difference can be noted in the O-grid but the main difference is in the radial and tangential directions in the free-stream cells.

## IV. Results

In this section a comparison is made between the three turbulence models, two DDES models; the original DDES<sub>8</sub> and the DDES<sub>16</sub> model, and the RANS model. The RANS simulation was performed using the S-A turbulence model. The effect of using the modified shielding function, presented in Eq. (5), is then analyzed.

In Fig. 5 the shielding function is compared between the DDES<sub>8</sub> and the DDES<sub>16</sub> models. The figure shows the instantaneous flow field at the MR surfaces presented in Fig. 3. It can be seen how the shielding function, for the

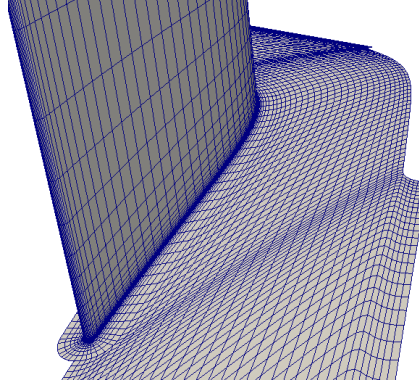


**Fig. 4** The mesh for the PSW blade passage. Every other grid line shown.

DDES<sub>8</sub> model, increases to unity inside the boundary layer at both pressure and suction sides. At the pressure side and approximately 50% of the suction side, the shielding function even reaches unity quite close to the wall, then drops down to zero for a small section of the boundary layer and increases back to one. Due to this behaviour the boundary layer is not well protected and is therefore solved in LES mode with inadequate mesh resolution. This will result in under predicted turbulent viscosity due to modelled stress depletion. This is, however, not the case for the DDES<sub>16</sub>, where the boundary layer is protected by the shielding function at the suction side. For the pressure side the shielding function seems, however, to extend too far out into the blade passage, as thinner boundary layer is expected there.

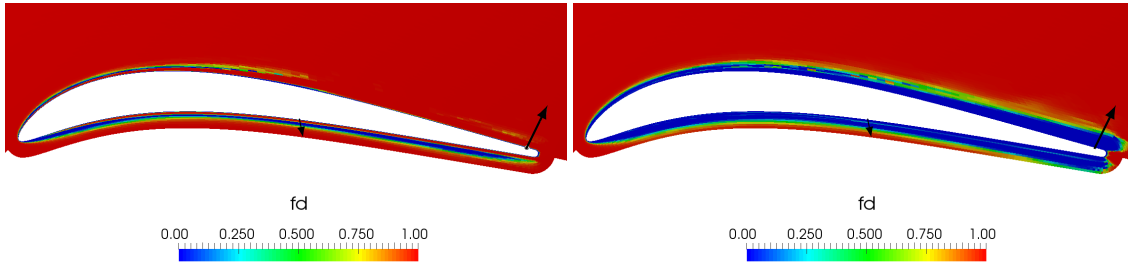


**Fig. 5** Shielding function at mid-span. DDES<sub>8</sub> on the left and DDES<sub>16</sub> on the right.

The behaviour at the suction side is further investigated by extracting profiles along the line at the trailing edge of the blade, shown as a black arrow in Fig. 5. Fig. 6 presents a comparison between RANS, DDES<sub>8</sub> and DDES<sub>16</sub>. The normalized S-A viscosity, normalized with the maximum value of the RANS S-A viscosity, is compared for all simulations. The shielding function is compared for the two DDES versions and the normalized velocity, obtained from the RANS simulations, is presented to be able to identify the boundary layer thickness. Here, the boundary layer thickness is defined as the distance from the wall where the flow has essentially reached the free-stream velocity. As can be seen in the figure, the viscosity is quite similar for the DDES<sub>16</sub> and the RANS models, where the difference in peak values is thought to be mainly due to the free-stream value of the S-A viscosity, but the LES mode breaks it down to a negligible value. For the DDES<sub>8</sub> model on the other hand, the viscosity is very low inside the boundary layer. The reason for this behaviour can be understood by viewing the trends of the shielding function, combined with the velocity profile from the RANS simulation. Ideally, the shielding function should be zero inside the boundary layer. As the figure shows, this is clearly the case for the DDES<sub>16</sub> model, whereas the shielding function for the DDES<sub>8</sub> model reaches unity almost instantaneously after leaving the wall. This causes the solver to enter LES mode inside the boundary layer, destroying the turbulent viscosity. For the DDES<sub>16</sub> model, by comparing the  $f_d$  function to the velocity profile, majority of the boundary layer is resolved in RANS mode. There is however a small bump in the DDES<sub>16</sub> shielding function outside of the boundary layer. This might be caused by some transient interactions between the boundary layer and transient flow features generated by the blade, e.g. vortices from the leading edge.

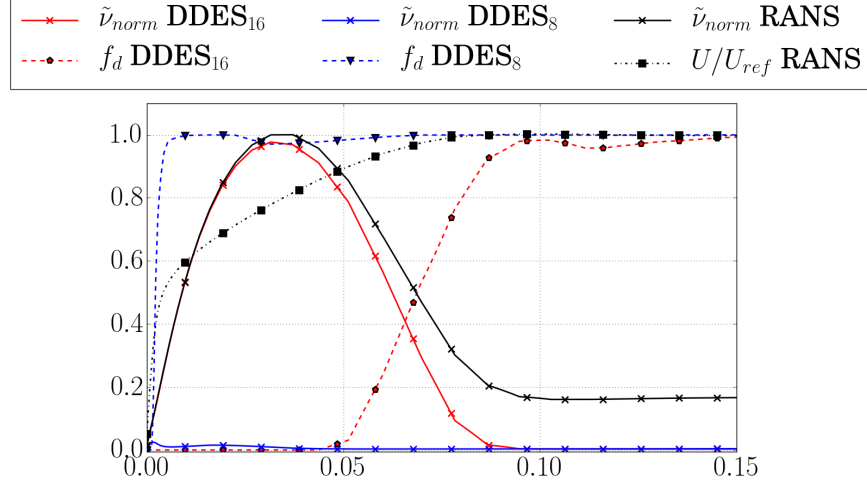


**Fig. 6** Shielding function performance at the trailing suction side. The x-axis is a normalized distance from the blade.

The performance of the shielding function at the pressure side is analyzed by considering the second black arrow, presented in Fig. 5, where the data is extracted from the O-grid. The resulting plot is shown in Fig. 7, where the same variables are plotted as before, with a new normalization. As before, the DDES<sub>8</sub> shielding function goes to unity almost instantaneously after the wall, resulting in very low S-A viscosity but now it fluctuates from one to zero towards the end of the boundary layer. There is a difference for the DDES<sub>16</sub> model as well, where the shielding function overpredicts the boundary layer thickness by large extent. The S-A viscosity is also underpredicted, compared to the RANS simulation. By following the shielding function, for the DDES<sub>16</sub> model, a small increase can be noticed near the end of the boundary layer, LES/RANS interface is expected. The shielding function is however broken down again, resulting in the incorrect prediction.

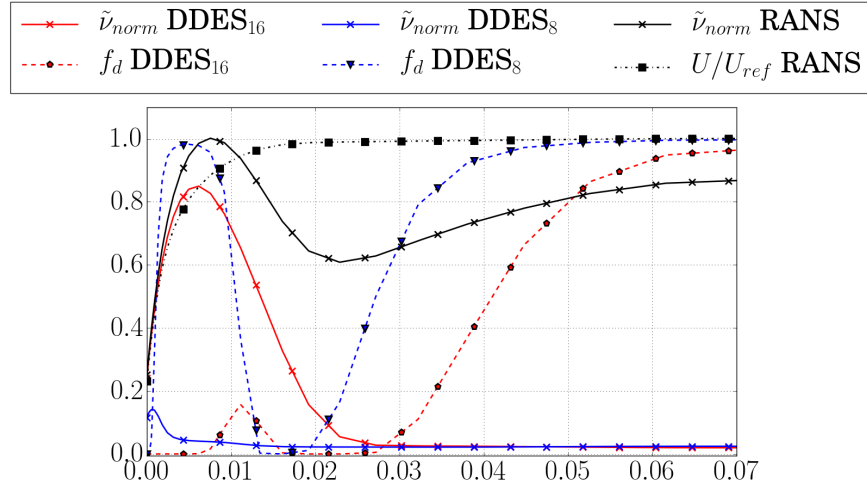


**Fig. 7** Shielding function performance at mid blade pressure side. The x-axis is a normalized distance from the blade.

So far, the modification has only been tested for the blade geometry, therefore the next step is to analyze the performance at the duct walls. Figure 8 shows the S-A viscosity contours at the FT surface, presented in Fig. 3. The figure, shows the DDES<sub>16</sub> to the left and the RANS simulation to the right (DDES<sub>8</sub> excluded as it shows very low uniform values that provide no additional information). The difference in S-A viscosity is caused by the fact that in the LES region the viscosity is broken down, explaining the large low viscosity regions in the DDES<sub>16</sub> figure.

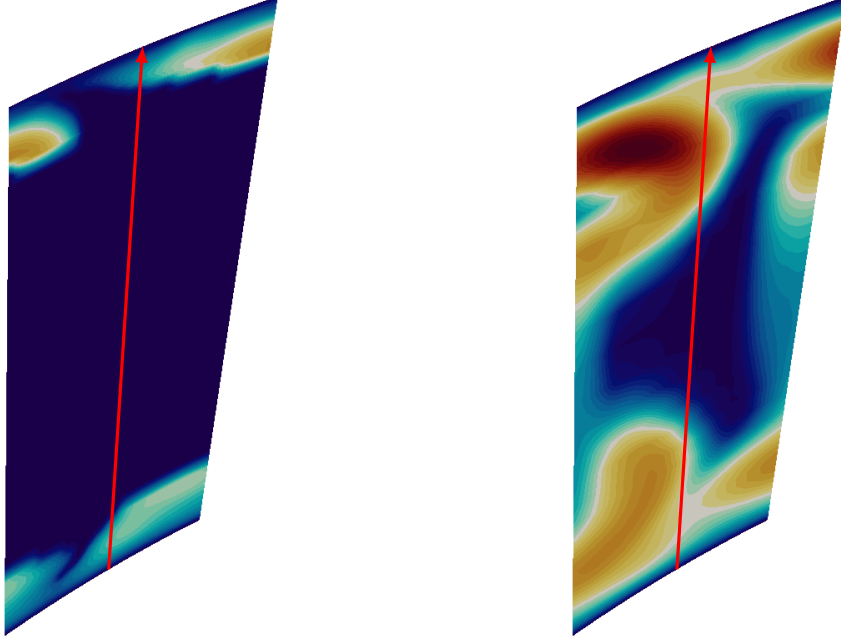


**Fig. 8** S-A viscosity contours at the FT surface. DDES<sub>16</sub> on the left and RANS on the right.

Instantaneous radial profiles at the axial location of the FT surface, shown as red arrows in Fig. 8, are presented in Fig. 9. The figure compares the same variables as in Fig. 6. The S-A viscosity is normalized with a different value than in Fig. 6 to have the two local peaks at unity. The main difference here, compared to the blade analysis, is the behaviour of the S-A viscosity for the RANS simulation, but the viscosity, both at hub and shroud, has two peaks. This might be explained by the wake traveling downstream from the PSW, which generates highly turbulent flow with strong vortices near both walls. For the RANS simulations those areas will have high values of S-A viscosity due to the modelled turbulence, referring back to Fig. 8.

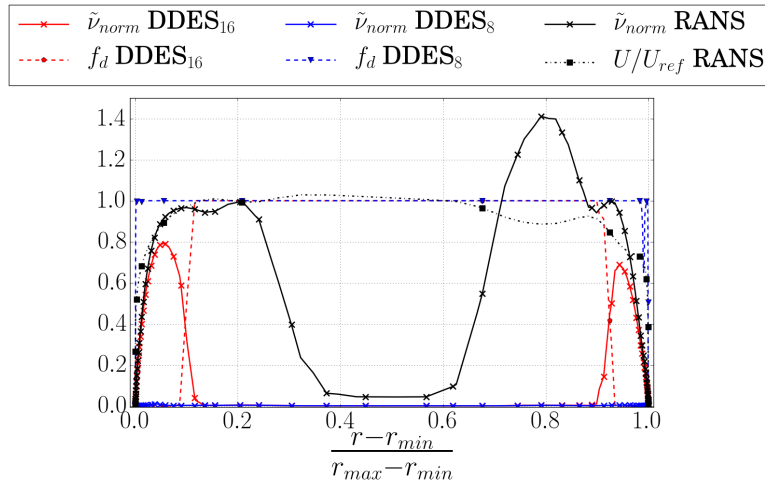


**Fig. 9** Shielding function performance for a specific tangential location, at the FT surface.

To be able to further analyze the duct walls behaviour of the radial profiles, an enlargement of Fig. 9, focusing on the near wall region, is illustrated in Fig. 10. The figure on the left shows the hub area whereas the one on the right shows the shroud area. The same variables are compared as before, in Fig. 9. In the figures a similar behaviour can be seen as for the blade profiles. The DDES<sub>8</sub> model underpredicts the turbulent viscosity due to an early switch from RANS to LES, resulting in the boundary layer being resolved in LES mode.

When moving over to the DDES<sub>16</sub> model, it is difficult to read into the behaviour in the shroud region due to the effects from the strong vortices, generated by the PSW. In the RANS simulation the S-A viscosity is increased due to those interaction effects, making it difficult to compare with the DDES model. This can be seen by considering the velocity profile where the boundary layer thickness is not clearly defined, resulting in an uncertainty regarding the shielding function performance. In the hub region, the behaviour is somewhat similar to what was experienced for the trailing edge of the PSW, at least when considering how the velocity profile extends from the wall. The S-A viscosity is however roughly 15% lower for the DDES<sub>16</sub> compared to the RANS simulation. This might, as for the shroud, be caused by the strong vortices, generated by the PSW, resulting in a much higher S-A viscosity for the RANS simulation in the free-stream of the duct, increasing it towards the outer regions of the boundary layer. The shielding function for the DDES<sub>16</sub> manages to protect the boundary layer where the velocity profile is quite stable, whereas protection from the DDES<sub>8</sub> model is still much too narrow, resulting in almost negligible S-A viscosity.

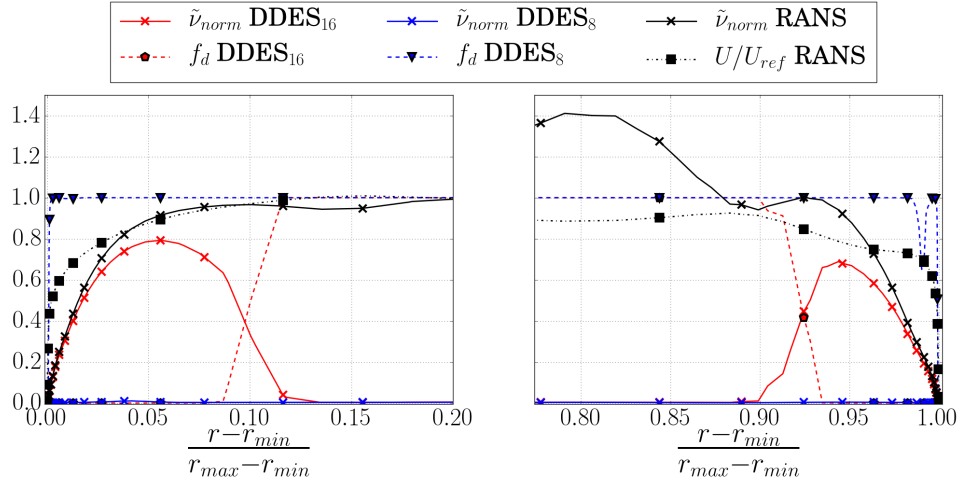


**Fig. 10** Zoomed in areas at hub (left) and shroud (right).

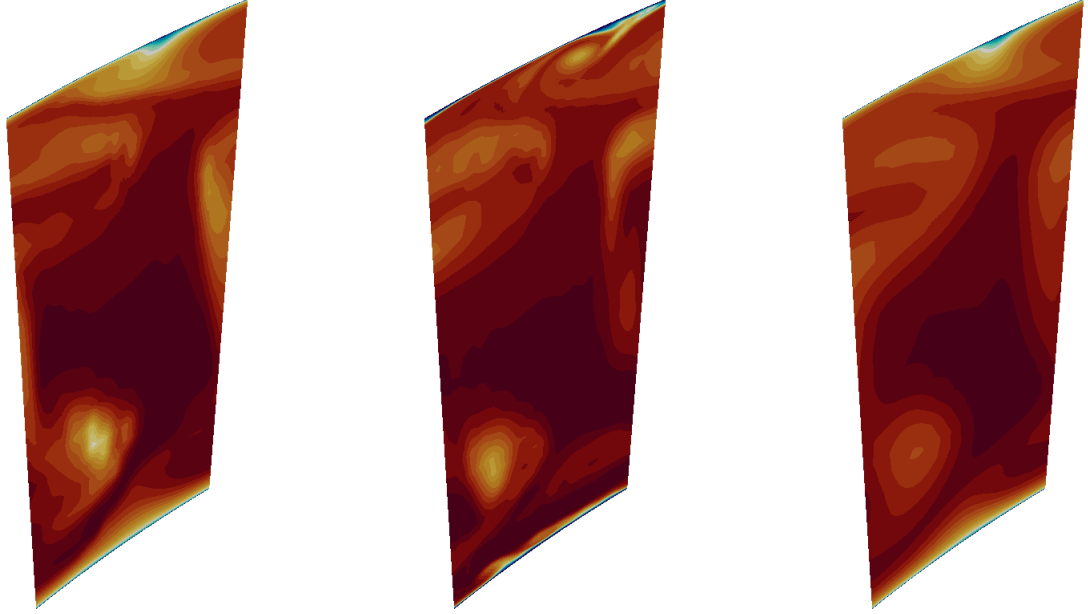
In Fig. 11 the velocity contours at the FT surface are presented for each of the models. The DDES<sub>16</sub> model is on the left, the DDES<sub>8</sub> is in the middle and the RANS is on the right. The contours from the DDES models are instantaneous while the RANS is time-averaged. All three figures show a similar structure, where the difference lies in the details and the scale, specially in the free-stream values. The shroud vortex is for example similar for the DDES<sub>16</sub> and the RANS simulation, whereas the DDES<sub>8</sub> has a bit different behaviour. The same goes for the hub region, where the DDES<sub>8</sub> model differs from the other two, resulting in a different boundary layer.

Figure 12 compares the normalized  $Q$ -criterion for the DDES<sub>16</sub> and the RANS simulation. This is done to show the difference in the resolved turbulence. As expected, the DDES<sub>16</sub> shows more detailed and smaller structures, specially towards the end of the domain, whereas the RANS simulation has no transient structures. For this comparison the DDES<sub>16</sub> was performed on the same mesh as used for the RANS simulation, which is relatively coarse, the full potential in resolving the turbulence is not exploited. This comparison still serves its purpose in comparing the resolved scales.

## V. Conclusion

A PSW from an experimental ICD test rig was simulated using the S-A DDES and RANS turbulence models. The study was conducted to determine the effect of a modified shielding function, compared to the original one, using the PSW blade geometry with the objective of, at a later stage, applying the model to the full test rig. Since the RANS region in the DDES model is solved in the same way as a full RANS simulation, the PSW was simulated using the S-A turbulence model for comparative reasons. In the DDES simulations the shielding function for the modified version, the DDES<sub>16</sub>, showed improvements in protecting the boundary layer for both the blade profile and the duct walls, though it was difficult to define the near shroud area with absolute certainty. However, for the pressure side of the blade, even though it was an improvement compared to the DDES<sub>8</sub> model, the DDES<sub>16</sub> model still overpredicted the boundary layer, although it resulted in a boundary layer solved using the RANS model. Due to this reasons, the DDES<sub>16</sub> model should be considered over the original for future simulations of the whole experimental rig. However, since the current study

was only performed on a simple blade profile with fully developed boundary layer, a similar study has to be performed for the whole rig simulation to assess the effects from different blade geometries, more complicated flow physics and boundary layer interaction with the unsteady flow features such as wakes and blade vortices.



**Fig. 11** Velocity contours comparison at the FT between the  $DDES_{16}$  (left),  $DDES_8$  (middle) and the RANS simulation (right).

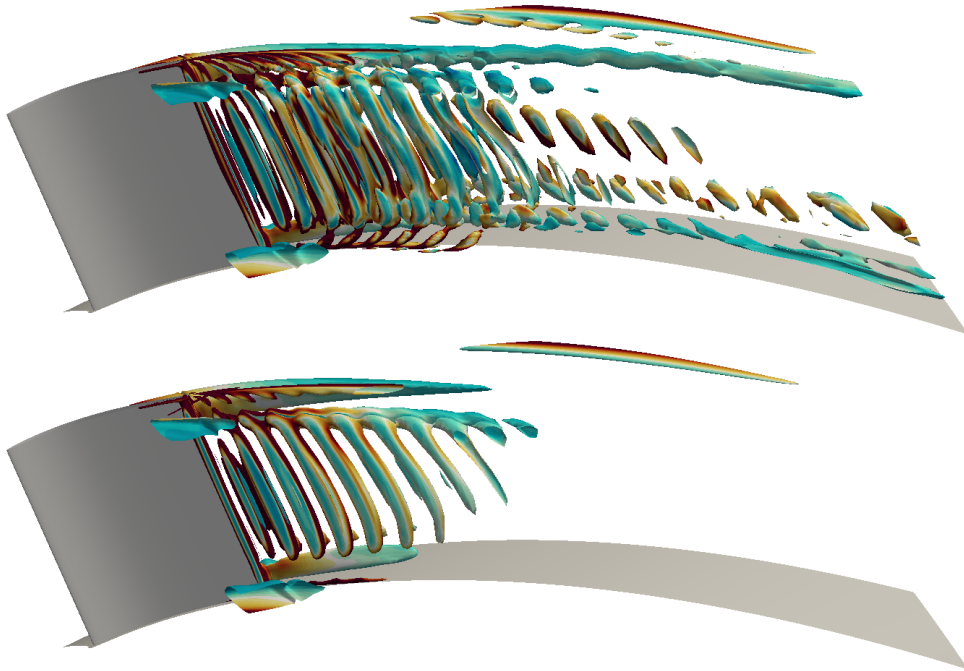


**Fig. 12** Iso-surfaces of the instantaneous, normalized  $Q$ -criterion,  $Q_{norm} = Qc/U^2$ , for the  $DDES_{16}$  (top) and the RANS simulation (bottom), colored by the vorticity magnitude.



## Acknowledgement

This research work was funded by the Swedish National Aviation Engineering Research Programme, NFFP with financial support from VINNOVA and the Swedish Defense Material Administration (FMV). All CFD simulations were performed using SNIC<sup>†</sup> resources at the National Supercomputer Center in Sweden, NSC.

## References

- [1] Amizadeh, F., Alonso, G., Benito, A., and Morales-Alonso, G., “Analysis of the recent evolution of commercial air traffic CO<sub>2</sub> emissions and fleet utilization in the six largest national markets of the European Union,” *Journal of Air Transport Management*, Vol. 55, 2016, pp. 9–19. doi:10.1016/j.jairtraman.2016.04.006.
- [2] Airbus, *Airbus GMF 2016-2035, Mapping Demand*, Art & Caractère, France, 2016.
- [3] JADC, “Worldwide Market Forecast 2016-2035,” Tech. Rep. YGR-5089, Japan Aircraft Development Corporation (JADC), Tokyo, Japan, 2016.
- [4] Ghisu, T., Parks, G. T., Jarret, J. P., and Clarkson, P. J., “An Integrated System for the Aerodynamic Design of Compressor Systems - Part II: Application,” *ASME. Journal of Turbomachinery*, Vol. 133, No. 1, 2010, pp. 011012–011012–8. doi:10.1115/1.4000535.
- [5] Ghisu, T., Parks, G. T., Jarret, J. P., and Clarkson, P. J., “An Integrated System for the Aerodynamic Design of Compressor Systems - Part I: Development,” *ASME. Journal of Turbomachinery*, Vol. 133, No. 1, 2010, pp. 011011–011011–10. doi:10.1115/1.4000534.
- [6] Naylor, E. M. J., Duenas, C. O., Miller, R. J., and Hodson, H. P., “Optimization of Nonaxisymmetric Endwalls in Compressor S-Shaped Ducts,” *ASME. Journal of Turbomachinery*, Vol. 133, No. 1, 2011, p. 011012. doi:10.1115/1.3103927.
- [7] Lu, H., Zheng, X., and Li, Q., “A combinatorial optimization design method applied to S-shaped compressor transition duct design,” *Journal of Aerospace Engineering*, Vol. 228, No. 10, 2014, pp. 1749–1758. doi:10.1177/0954410014531922.
- [8] Donghai, J., Xiwu, L., Weiguang, Z., and Xingmin, G., “Optimization of endwall contouring in axial compressor S-shaped ducts,” *Chinese Journal of Aeronautics*, Vol. 28, No. 4, 2015, pp. 1076–1086. doi:10.1016/j.cja.2015.06.011.
- [9] Walker, A. D., Barker, A. G., and Carrotte, J. F., “Numerical design and experimental evaluation of an aggressive s-shaped compressor transition duct with bleed,” *ASME Turbo Expo: Power for Land, Sea, and Air*, Vol. 7: Turbomachinery, Parts A, B and C, American Society of Mechanical Engineers, 2011, pp. 151–161. doi:10.1115/GT2011-45628.
- [10] Walker, A. D., Barker, A. G., Carrotte, J. F., Bolger, J. J., and Green, M. J., “Integrated Outlet Guide Vane Design for an aggressive S-Shaped Compressor Transition Duct,” *ASME. Journal of Turbomachinery*, Vol. 135, No. 1, 2012, pp. 011035–011035–11. doi:10.1115/1.4006331.
- [11] Gao, L., Deng, X., Feng, X., and Yang, Z., “Effect of inlet conditions on compressor intermediate duct,” *Journal of Aerospace Engineering*, Vol. 229, No. 6, 2014, pp. 1154–1168. doi:10.1177/0954410014542624.
- [12] Bailey, D. W., Britchford, K. M., Carrotte, J. F., and Stevens, S. J., “Performance Assessment of an Annular S-Shaped duct,” *ASME. Journal of Turbomachinery*, Vol. 119, No. 1, 1997, pp. 149–156. doi:10.1115/1.2841003.
- [13] Britchford, K. M., Carrotte, J. F., Stevens, S. J., and McGuirk, J. J., “The development of the mean flow and turbulence structure in an annular S-shaped duct,” *ASME. Turbo Expo: Power for Land, Sea, and Air*, Vol. 1, No. 1: Turbomachinery (V001T01A144), 1994, p. V001T01A144. doi:10.1115/94-GT-457.
- [14] Britchford, K., Manners, A. P., McGuirk, J., and Stevens, S., “Measurement and prediction of flow in annular S-shaped ducts,” *Experimental Thermal and Fluid Science*, Vol. 9, No. 2, 1994, pp. 197–205. doi:10.1016/0894-1777(94)90112-0.
- [15] Spalart, P. R., Deck, S., Shur, M. L., Squires, K. D., Strelets, M. K., and Travin, A., “A new version of detached-eddy simulation, resistant to ambiguous grid densities,” *Theoretical Computational Fluid Dynamics*, Vol. 20, 2006, pp. 181–195. doi:10.1007/s00162-006-0015-0.
- [16] Ashton, N., West, A., and Mendonça, F., “Flow Dynamics Past a 30P30N Three-Element Airfoil Using Improved Delayed Detached-Eddy Simulation,” *AIAA Journal*, Vol. 54, No. 11, 2016, pp. 3657–3667. doi:10.2514/6.2017-4281.
- [17] Ashton, N., “Recalibrating Detached-Eddy Simulation to eliminate modelled-stress depletion,” *23rd AIAA Computational Fluid Dynamics Conference, AIAA AVIATION Forum*, AIAA, 2017, pp. 1–15. doi:10.2514/6.2017-4281.

---

<sup>†</sup>Swedish National Infrastructure for Computing



- [18] Probst, A., Radespiel, R., Wolf, C., Knopp, T., and Schwamborn, D., "A Comparison of Detached-eddy Simulation and Reynolds-stress Modelling Applied to the Flow over a Backward-facing Step and an Airfoil at Stall," *48th AIAA Aerospace Sciences Meeting Including the New Horizons Forum and Aerospace Exposition, Aerospace Sciences Meetings*, AIAA, 2010, pp. 1–18. doi:doi:10.2514/6.2010-920.
- [19] Eriksson, L.-E., "Development and Validation of Highly Modular Flow Solver Versions in G2DFLOW and G3DFLOW," Tech. Rep. 9970-1162, Volvo Aero Corporation, 1995. Volvo Aero Corporation.
- [20] Andersson, N., Eriksson, L.-E., and Davidson, L., "Large-Eddy Simulation of Subsonic Turbulent Jets and Their Radiated Sound," *AIAA Journal*, Vol. 43, No. 9, 2005, pp. 1899–1912.
- [21] Spalart, P. R., Jou, W.-H., Strelets, M., and Allmaras, S. R., "Comments on the Feasibility of LES for Wings, and on a Hybrid RANS/LES Approach," *Proceedings of first AFOR International Conference on DNS/LES*, Greyden Press, Ruston, Louisiana, 1997, pp. 137–147. Edited by C. Liu and Z. Liu.
- [22] Spalart, P. R., and Allmaras, S. R., "A one-equation turbulence model for aerodynamic flows," *30th Aerospace Sciences Meeting and Exhibit, Aerospace Sciences Meetings*, Vol. 1, 1992, pp. 5–21. doi:10.2514/6.1992-439.
- [23] Shur, M., Spalart, P. R., Strelets, M., and Travin, A., "Detached-eddy simulation of an airfoil at high angle of attack," *Engineering Turbulence Modelling and Experiments 4*, Vol. 4, 1999, pp. 669–678. doi:10.1016/B978-008043328-8/50064-3.
- [24] Vatsa, V. N., Lockard, D. P., and Spalart, P. R., "Grid Sensitivity of SA-Based Delayed-Detached-Eddy-Simulation Model for Blunt-Body Flows," *AIAA Journal*, Vol. 55, No. 8, 2017, pp. 2842–2847. doi:10.2514/1.J055685.
- [25] Spalart, P. R., Johnson, F. T., and Allmaras, S. R., "Modifications and Clarifications for the Implementation of the Spalart-Allmaras Turbulence Model," *Seventh International Conference on Computational Fluid Dynamics (ICCFD7)*, Haway, 2012.
- [26] Spalart, P. R., "Young-Person's Guide to Detached-Eddy Simulation Grid," Tech. Rep. NASA/CR-2001-211032, NASA Langley Technical Report Server, Moffett Field, CA, USA, 2001.